Research Article

Nano Research
2022, 15(1): 162–169

ISSN 1998-0124 CN 11-5974/O4
https://doi.org/10.1007/s12274-021-3451-7

Strengthen metal-oxygen covalency of CoFe-layered double hydroxide for efficient mild oxygen evolution

Dazhong Zhong[1,§], Tan Li[2,§], Dong Wang[1], Lina Li[3], Jiancheng Wang[4], Genyan Hao[1], Guang Liu[1], Qiang Zhao[1] (✉), and Jinping Li[1,4] (✉)

[1] College of Chemistry and Chemical Engineering, Taiyuan University of Technology; Shanxi Key Laboratory of Gas Energy Efficient and Clean Utilization, Taiyuan 030024, China
[2] School of Environment and Energy, South China University of Technology, Guangzhou 51006, China
[3] Shanghai Synchrotron Radiation Facility, Shanghai Advanced Research Institute, Shanghai 200000, China
[4] Key Laboratory of Coal Science and Technology, Taiyuan University of Technology, Ministry of Education and Shanxi Province, Taiyuan 030024, China
[§] Dazhong Zhong and Tan Li contributed equally to this work.

© Tsinghua University Press and Springer-Verlag GmbH Germany, part of Springer Nature 2021

Received: 30 October 2020 / **Revised:** 10 March 2021 / **Accepted:** 11 March 2021

ABSTRACT

Oxygen evolution reaction (OER) is crucial for hydrogen production as well as other energy storage technologies. CoFe-layered double hydroxide (CoFe-OH) has been widely considered as one of the most efficient electrocatalysts for OER in basic aqueous solution. However, it still suffers from low activity in neutral electrolyte. This paper describes partially oxidized CoFe-OH (PO-CoFe-OH) with enhanced covalency of M-O bonds and displays enhanced OER performance under mild condition. Mechanism studies reveal the suitably enhanced M-O covalency in PO-CoFe-OH shifts the OER mechanism to lattice oxygen oxidation mechanism and also promotes the rate-limiting deprotonation, providing superior OER performance. It just requires the overpotentials of 186 and 365 mV to drive the current density densities of 1 and 10 mA·cm^{-2} in 0.1 M $KHCO_3$ aqueous solution (pH = 8.3), respectively. It provides a new process for rational design of efficient catalysts for water oxidation in mild conditions.

KEYWORDS

lattice oxygen oxidation, metal-oxygen covalency, neutral, oxygen evolution reaction

1 Introduction

Electrocatalytic water splitting into oxygen and hydrogen, which is powered by renewable energy, plays a central role in clean energy harvest, storage, and utilization [1, 2]. However, it needs considerable energy consumption to drive the critical half-reaction, the sluggish oxygen evolution reaction (OER) ($2H_2O \rightarrow O_2 + 4H^+ + 4e^-$) with the complex proton-electron transfer process [1–3]. Catalysts are urgently required to accelerate the reaction kinetics and decrease the overpotential and energy consumption efficiently [1–4].

Especially, OER under mild conditions, which can direct electrolyze seawater for hydrogen production or couple the CO_2 reduction reaction for CO_2 conversion, is promising for large-scale environmentally friendly practical applications. Boosting the OER activity in (near-)neutral electrolyte is urgently demanded. Since 2008, Kanan et al. reported *in situ* formation of cobalt-phosphate (Co-Pi) in 0.1 M KPi aqueous solution (pH = 7) containing Co^{2+} for efficient oxygen evolution, showing a current density of ~ 1.25 mA·cm^{-2} at 1.29 V vs. the standard hydrogen electrode [5, 6]. After that, Ni-Bi was prepared similarly and exhibited an overpotential of ~ 425 mV at a current density of 1 mA·cm^{-2} in 0.1 M $K_2B_4O_7$ aqueous solution at pH 9.2 [7]. Furthermore, Co-Bi [8], CoP@Co-Bi-Pi [9], Ni-Bi [10], and $Co_3(PO_4)_2$ nanosheet [11], etc. [12–14] were developed and showed high OER activities in mild conditions.

Because of the attractive two-dimensional lamellar structure and easily tunable metal centers, layered double hydroxides (LDHs) have been revealed as promising OER catalysts over the past few decades [15–22]. In particular, CoFe-layered double hydroxide (CoFe-OH) has been revealed as one of the most efficient OER catalysts [23–26]. However, it generally operates in a basic aqueous solution, the activity in (near-)neutral oxygen evolution electrolysis still needs to be improved [27]. Transition-metal oxyhydroxides can form *in situ* on the catalyst during oxygen evolution electrolysis in basic aqueous solution and are accepted as efficient OER catalysts [28–32]. However, it is a challenge to generate transition-metal oxyhydroxides in the (near-)neutral electrolyte, thus resulting in an inferior OER performance [33–35]. We thus predict that transforming CoFe-OH in an alkaline electrolyte can significantly enhance its performance in (near-)neutral electrolytes.

In addition, although the presence of transition-metal oxyhydroxides has been proposed to promote OER activity, the role is still ambiguous and not well understood, because the as-prepared catalyst is unstable and usually different from that under OER in a basic electrolyte. Hence, it is hard to

Address correspondence to Qiang Zhao, zhaoqiang@tyut.edu.cn; Jinping Li, jpli211@hotmail.com

establish a structure-activity relationship [36]. A relatively stable structure in mild condition may help to understand the mechanism further.

Because CoFe-OH is one of the most efficient electrocatalysts for OER, we employed CoFe-OH as an example catalyst in our experiment. CoFe-OH, partially oxidized CoFe-OH (PO-CoFe-OH), and highly oxidized CoFe-OH (HO-CoFe-OH) were prepared for study. We found that PO-CoFe-OH gave a better activity than HO-CoFe-OH and the original CoFe-OH. The slightly enhanced M-O covalent bond in PO-CoFe-OH promoted lattice oxygen oxidation and facilitated the deprotonation for OER.

2 Experimental

2.1 Materials

Potassium hydrogen carbonate ($KHCO_3$, ≥ 99.5%) was obtained from Guangfu Co., Ltd. (Tianjin, China). Iron nitrate nonahydrate ($Fe(NO_3)_3{\cdot}9H_2O$, analytical reagent (AR)) was purchased from Sinopharm. Cobalt nitrate hexahydrate ($Co(NO_3)_2{\cdot}6H_2O$, AR), Urea (AR, 99%), ammonium fluoride (NH_4F, 99.99%), and potassium hydroxide (KOH, AR) were obtained from Aladdin Ltd. (Shanghai, China).

2.2 Preparation of CoFe-OH, PO-CoFe-OH, HO-CoFe-OH, and $Co^{II}_{0.47}Fe^{III}_{0.53}O_xH_y$

CoFe-OH was prepared by a hydrothermal method [37]. Typically, $Co(NO_3)_2{\cdot}6H_2O$ (0.5 mmol), $Fe(NO_3)_3{\cdot}9H_2O$ (0.5 mmol), urea (5 mmol), and NH_4F (2 mmol) were dissolved in DI water (18 mL) to form a precursor solution. Subsequently, the prepared solution was transferred into a Teflon-lined (23 mL) stainless steel vessel. After that, the NF (2 cm × 3 cm) was vertically placed in the vessel and then maintained at 120 °C for 6 h. After cooling to room temperature, the CoFe-OH on NF was rinsed with DI water and ethanol, and then dried at 60 °C for 12 h. To prepare PO-CoFe-OH, CoFe-OH (1 cm^2) was employed as the anode and treated through cyclic voltammetry (CV) in 1 M KOH (60 mL) at the potential window of 0–1 V vs. Hg/HgO with a scan rate of 50 $mV{\cdot}s^{-1}$ to reach a stable state. Pt mesh was employed as the counter electrode. The preparation of HO-CoFe-OH is similar to that of PO-CoFe-OH except that 1 M KOH was replaced by 8.8 M KOH. The catalyst loadings were determined by weighing the mass of bare NF and that NF with catalysts. The loadings of CoFe-OH, PO-CoFe-OH, and HO-PO-CoFe were ca. 2.4, 1.9, and 1.6 $mg{\cdot}cm^{-2}$, respectively. The loading of PO-CoFe-OH and HO-CoFe-OH was slightly reduced due to the fall off during the preparation.

$Co^{II}_{0.47}Fe^{III}_{0.53}O_xH_y$ was prepared by electrodeposition through the NO_3^- reduction induced pH rise. The electrodeposition was conducted in 80 mL electrolyte with 50 mM $Co(NO_3)_2$ and 35 mM $Fe(NO_3)_3$ at −1 V vs. Ag/AgCl for 300 s. The molar ratio of Co/Fe was determined to be 0.47/0.53 by inductively coupled plasma-optical emission spectroscopy (ICP-OES). The loading of $Co^{II}_{0.47}Fe^{III}_{0.53}O_xH_y$ is ca. 1.8 $mg{\cdot}cm^{-2}$.

2.3 Material characterization

X-ray diffraction (XRD) patterns and scanning electron microscopy (SEM) images were obtained from a Bruker D8 advance diffractometer (Cu-Kα radiation, λ = 1.5418 Å) and a Hitachi SEM (SU8010, Japan), respectively. Transmission electron microscopy (TEM) images were carried out on a JEOL-2100F instrument (Japan, 200 kV). X-ray photoelectron spectroscopy (XPS) analysis was conducted on an ESCALAB 220i-XL spectrometer (VG Scientific, Sussex, UK) with Al-Kα radiation ($h\nu$ = 1,486.6 eV, 150 W). Raman spectra were obtained on a Renishaw Raman spectrometer equipped with a green laser (532 nm).

2.4 Electrochemical measurements

The electrochemical measurements were performed in a standard three-electrode system connected to a Princeton electrochemical workstation (PARSTAT MC, Princeton, Oak Ridge, TN, USA). Ag/AgCl (saturated with KCl) and Pt mesh were employed as reference electrode and counter electrode, respectively. Linear sweep voltammetry (LSV) curves were collected in 0.1 M $KHCO_3$ at a scan rate of 2 $mV\ s^{-1}$. All of the potentials were converted to the reversible hydrogen electrode scale by the equation: E (V vs. RHE) = E (V vs. Ag/AgCl) + 0.197 + 0.059 × pH. iR-drop compensation was added except for that mentioned. Electrochemical impedance spectroscopy (EIS) data were collected under the frequency range of 100 kHz to 0.05 Hz. Before the electrochemical test, the potential of Ag/AgCl reference electrode was checked by measuring the open circuit potential with the as-received standard Ag/AgCl electrode in 0.1 M KCl aqueous solution. The open circuit potential between Ag/AgCl reference electrode and standard Ag/AgCl should less than 1 mV.

2.5 Operando Raman spectroscopy test

Operando Raman spectroscopy was collected in a custom-built Teflon cell (Shanghai Chuxi Industrial Co., Ltd.) connected with an electrochemical workstation (CHI660E) (Fig. S26 in the Electronic Supplementary Material (ESM)). Pt wire and Ag/AgCl (3.5 M KCl) were employed as counter electrode and reference electrode, respectively. The electrolyte was 0.1 M $KHCO_3$ aqueous solution. The Raman spectra were collected at 1.3 and 1.5 V vs. RHE (without iR-drop compensation) by the spectrometer equipped with a green laser (532 nm).

2.6 Computational details

In this paper, the density functional theory (DFT) plus Hubbard-U (DFT + U) methods with a plane wave basis set through CASTEP module [38] were employed to view the free energy variation for O_2 evolution on CoFe-LDH/CoFeOOH interfaces. Meanwhile, the H_2O solvation models built through amorphous cell were introduced to simulate the affection from the solvents. Here, the effective U was fixed as 4.4 eV, 6.4 eV, and 4.3 eV for Co^{2+}, Co^{3+}, and Fe, respectively [18, 39]. The Perdew–Burke–Ernzerhof (PBE) function of generalized gradient approximation (GGA) as exchange–correlation potential was adopted for the geometry optimization [40]. The ionic cores were pictured with norm conserving pseudopotential with a plane-wave basis cutoff energy of 900 eV, and the way relativistic effects were incorporated into Koelling-Harmon. The Brillouin zone integrations were approximated using the special k-point sampling scheme of Monkhorst-Pack [41, 42]. The k-point grids were used with 4 × 4 × 2 for primitive cell and the supercell was built with 4 × 4 × 1 range with 1 × 1 × 1 k-point grids calculations. The density mixing minimization method was selected for the electronic minimizer. The convergence was assumed when the convergence tolerance of energy, maximum force, and maximum displacement were respective less than 5.0×10^{-5} $eV{\cdot}atom^{-1}$, 0.03 $eV{\cdot}Å^{-1}$, and 1.0×10^{-3} Å.

Adsorbed groups and the top three atomic layers were allowed to relax to the minimum in the enthalpy without any constraints. The vacuum space along the z-direction was set to be 15 Å, which is enough to avoid interaction between the two neighboring images.

Free energy change (ΔG) of the reaction was calculated as the difference between the free energies of the initial and final

states as shown below:

$$\Delta G = \Delta E + \Delta ZPE - T\Delta S$$

where E, ZPE, and S are the calculated energies by DFT, the zero-point energy, and the entropy, respectively.

3 Results and discussion

3.1 Structural characterization

CoFe-OH was prepared on nickel foam by a hydrothermal strategy (Fig. S1(a) in the ESM). The XRD pattern shows typical diffraction peaks of CoFe-LDH, revealing the successful preparation of CoFe-OH (Fig. S2 in the ESM) [23]. As shown in Fig. S3 in the ESM, SEM and TEM images demonstrate that the layered CoFe-OH was obtained. The lattice distances of 2.66 ± 0.03 Å, which correspond to (012) facet of CoFe-OH, were observed in the high-resolution TEM (HR-TEM) image (Figs. S3(c), S4, and S11 in the ESM). Energy-dispersive X-ray spectroscopy (EDS) mapping and line scanning confirmed the homogeneous distribution of Co, Fe, and O elements (Figs. S3(d) and S3(e) in the ESM).

PO-CoFe-OH and HO-CoFe-OH were fabricated by oxidizing CoFe-OH through CV in 1 M KOH and 8.8 M KOH, respectively, at the potential window of 0–1 V vs. Hg/HgO for several cycles to reach a stable state (Fig. 1(a)). XRD patterns show the inferior crystallinity of PO-CoFe-OH and HO-PO-CoFe, implying CoFe-OH was oxidized and converted into long-range disordered CoFe oxyhydroxide (Fig. S2 in the ESM). CoFe oxyhydroxide has been previously revealed as a stable state under open circuit [25]. The long-range disordered structure has been mentioned to boost the electrochemical surface area of the catalysts and facilitate OER [37, 43]. XRD patterns were collected at lower scan rates to gain more crystalline information of PO-CoFe-OH and HO-CoFe-OH (Fig. S5 in the ESM). It can be found in Fig. S5 in the ESM that all diffraction peaks shifted to higher degrees from CoFe-OH to PO-CoFe-OH and HO-CoFe-OH. The results indicate a gradual decrease of the atom distance along with the conversion of CoFe-OH to PO-CoFe-OH and HO-CoFe-OH. SEM and TEM characterization revealed that the morphology of PO-CoFe-OH was maintained and still presented as the nanosheet structure (Fig. S6 in the ESM). Meanwhile, HR-TEM image shows that PO-CoFe-OH is short-range ordered, and the lattice distance of (012) is slightly reduced to 2.46 ± 0.07 Å (Fig. 1(b) and Fig. S11 in the ESM). Besides, elemental mapping and line scanning profile reveal that the Co, Fe, and O elements are uniformly distributed (Fig. 1(c) and Fig. S7 in the ESM). As displayed in Figs. S8(a)–S8(c) in the ESM, SEM and TEM images also reveal a similar sheet-like structure of HO-CoFe-OH. EDS mapping and line scanning profile also indicate the uniform distribution of Co, Fe, and O elements (Figs. S8(d)–S8(f) in the ESM). The layer thickness of the catalysts was determined by atomic force microscope (AFM). CoFe-OH, PO-CoFe-OH, and HO-CoFe- OH show a similar thickness of ca. 5 nm (Fig. S9 in the ESM). ICP-OES analysis confirms that the contents of Co and Fe are slightly reduced from CoFe-OH to HO-CoFe-OH, similar to the change of catalysts loading mentioned above, and the molar ratios of Co/Fe are close to 1 in all three samples (Table S1 in the ESM). The lattice distance of (012) in HO-CoFe-OH was further reduced to 2.36 ± 0.02 Å, evidenced by the HR-TEM image (Figs. S10 and S11 in the ESM). The decrease of the lattice distance can be attributed to the shortening of M-O covalent bond derived from the strengthen of M-O covalency (details are shown below).

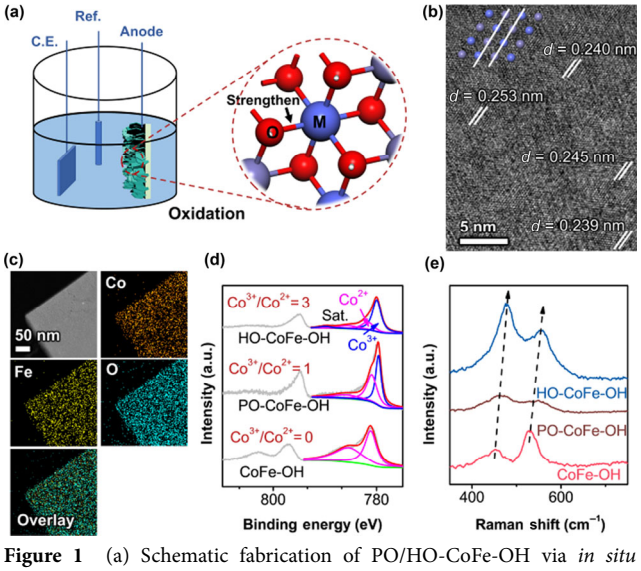

Figure 1 (a) Schematic fabrication of PO/HO-CoFe-OH via *in situ* conversion of CoFe-OH in KOH aqueous solution. (b) HR-TEM image of PO-CoFe-OH, inset in the top left corner shows the metal atoms arrangement model. (c) High-angle annular dark-field TEM (HAADF-TEM) image and element mapping of PO-CoFe-OH. (d) Co XPS spectra and (e) Raman spectra of CoFe-OH, PO-CoFe-OH, and HO-CoFe-OH.

XPS was performed to reveal the chemical states of Co, Fe, and O. As shown in Fig. 1(d), the percentage of Co^{3+} for CoFe-OH, PO-CoFe-OH, and HO-CoFe-OH are increased from 0 to ca. 50% and ca. 75%, respectively (Co^{3+} at ca. 779.8 eV and Co^{2+} at ca. 781.3 eV) [44–46]. As displayed in Fig. S12 in the ESM, Fe elements are in the valence of +3 in all samples [44]. The peak of O^{2-} increased in PO-CoFe-OH and HO-CoFe-OH, demonstrating the formation of CoFe oxyhydroxide (Fig. S13 in the ESM) [29, 47]. Furthermore, Raman spectra were employed to evaluate the structure of the catalyst further. As displayed in Fig. 1(e), two peaks centered at ca. 453 and 528 cm^{-1}, which were assigned to the stretching modes of M-O, were observed for CoFe-OH [48, 49]. The peak at lower wavenumber became slightly more prominent after oxidation in 1 M KOH, demonstrating CoFe-OH was partially converted to CoFeOOH [50]. As the concentration of the treating KOH solution further increased to 8.8 M, the peaks shifted to an even higher wavenumber, and the peak at lower wavenumber became more prominent, implying CoFe-OH was highly oxidized to CoFeOOH [50]. Obviously, the Raman peaks shifted to higher wavenumbers from CoFe-OH to PO-CoFe-OH and then HO-CoFe-OH, which powerfully demonstrate that M-O covalent bonds were enhanced associated with the oxidation of CoFe-OH [51–53], agreeing well with the decreased lattice distance evidenced by XRD patterns and HR-TEM images. As the lamellar structure of CoFe-OH may disappear in PO/HO-CoFe-OH, it may affect the Raman spectra. To exclude the effect of lamellar structure on Raman spectra, we compared the Raman spectra of CoFe-OH before and after exfoliation. The exfoliation of the CoFe-OH was obtained by dispersion of the CoFe-OH powder in formamide with a concentration of 1 mg·mL^{-1} under N_2 flow. We find the Raman spectra of exfoliated CoFe-OH is similar to the as-prepared CoFe-OH, confirming the shift of Raman spectra is caused by the strengthen of M-O covalency (Fig. S14 in the ESM).

Moreover, we also conducted X-ray absorption spectroscopy (XAS) to further illustrate the structure of the catalysts (Fig. 2, and Figs. S15–S21 in the ESM). As shown in Fig. 2(a), the Co K-edge X-ray absorption near edge structure (XANES) spectrum of CoFe-OH gives a pre-edge feature at 7,709.5 eV and a sharp intense white line at 7,727.3 eV, clearly indicating a dominating

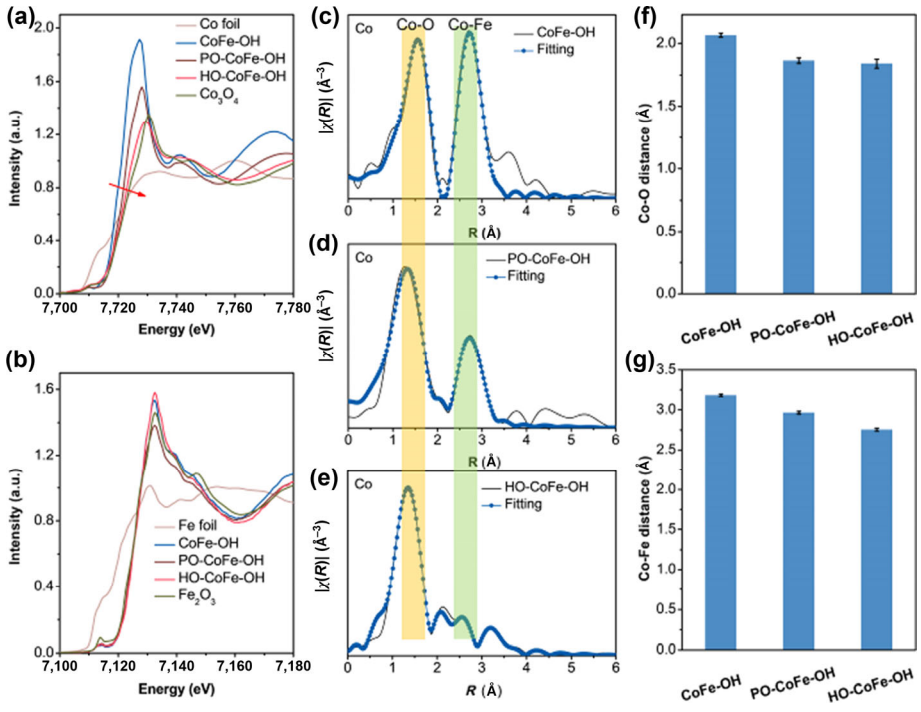

Figure 2 (a) Co K-edge and (b) Fe K-edge XANES spectra of CoFe-OH, PO-CoFe-OH, and HO-CoFe-OH. (c)–(e) Fourier transform of Co K-edge, (f) Co-O distance, and (g) Co-Fe distance of CoFe-OH, PO-CoFe-OH, and HO-CoFe-OH.

contribution of Co^{2+} in octahedral coordination [25]. The binding energy of Co K-edge shifts to higher values from CoFe-OH to PO-CoFe-OH and then HO-CoFe-OH, demonstrating the valence of Co gives an incremental trend. The XANES results further reveal the formation of CoFeOOH in PO/HO-CoFe-OH. Fe K-edge show that the valence states of Fe are the same as +3 valence, which is also consistent with the XPS results (Fig. 2(b)). The Fourier transform of the extended X-ray absorption fine structure spectroscopy (EXAFS) was employed to explore the atomic configuration of the samples. In the Co(Fe) *R*-space spectra (Figs. 2(c)–2(g) and Figs. S15–S20 in the ESM), the peaks centered at 2–3 Å originate from the Co-Fe shell and the peaks centered at 1–2 Å from the Co(Fe)-O shell. The Co(Fe)-O distance and Co-Fe distance appeared with a decreased trend from CoFe-OH to PO-CoFe-OH and then HO-CoFe-OH, further demonstrating the enhanced covalency of M-O bond associated with the conversion of CoFe-OH to CoFeOOH [25, 54]. We also note that the contribution of Co-Fe shell possesses a decreasing trend from CoFe-OH to PO-CoFe-OH and then HO-CoFe-OH, revealing the structure becomes long-range disordered associated with the contraction of the M-O bond.

3.2 Oxygen evolution reaction performance

The OER performance of CoFe-OH, PO-CoFe-OH, and HO-CoFe-OH were evaluated in 0.1 M $KHCO_3$ solution using a standard three-electrode system with Ag/AgCl (saturated KCl) as the reference electrode and Pt mesh as the counter electrode. PO-CoFe-OH needs an overpotential of only 186 mV to drive a current density of 1 mA·cm^{-2}, which is 48 and > 184 mV lower than HO-CoFe-OH and CoFe-OH, respectively, demonstrating the superior OER performance of PO-CoFe-OH (Fig. 3(a)).

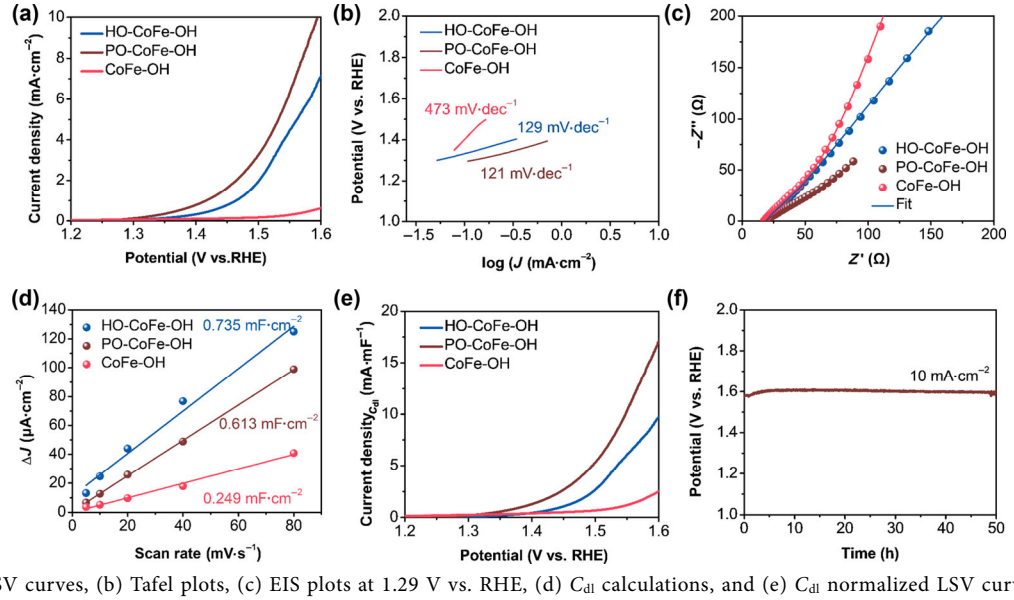

Figure 3 (a) LSV curves, (b) Tafel plots, (c) EIS plots at 1.29 V vs. RHE, (d) C_{dl} calculations, and (e) C_{dl} normalized LSV curves of CoFe-OH, PO-CoFe-OH, and HO-CoFe-OH. (f) Stability test of PO-CoFe-OH at the current density of 10 mA·cm^{-2}.

In addition, PO-CoFe-OH just needs an overpotential of 365 mV to drive a current density of 10 mA·cm^{-2}, which is superior to most of the reported catalysts (Table S4 in the ESM). Consistently, the Tafel-slope analysis reveals the faster mass-transfer kinetics of PO-CoFe-OH (Fig. 3(b)). EIS analysis also revealed PO-CoFe-OH exhibits a smaller charge transfer resistance (Fig. 3(c) and Figs. S22–S24).

The electrochemical surface area (ECSA) is a critical factor to impact the catalytic performance. Double-layer capacitance (C_{dl}) was conducted to represent the ECSA. As shown in Fig. 3(d) and Fig. S25 in the ESM, the HO-CoFe-OH had a C_{dl} value of 0.735 mF·cm^{-2}, which is ca. 1.2 and 3.0 times of that of PO-CoFe-OH (0.613 mF·cm^{-2}) and CoFe-OH (0.249 mF·cm^{-2}), respectively. The results are consistent with that the long-range disordered structure could help to expose more active sites and promote OER activity [37, 43]. It is critical to exclude the effects of ECSA for further understanding the intrinsic OER of the catalysts. The LSV curves were normalized by C_{dl} and shown in Fig. 3(e) [55]. The results showed that PO-CoFe-OH gave the most efficient intrinsic activity, followed by HO-CoFe-OH and CoFe-OH. We also evaluated the mass activity of these catalysts (Fig. S26 in the ESM). The results also revealed PO-CoFe-OH exhibited the best mass activity. The LSV curves normalized by the contents of Co and Fe further evidenced PO-CoFe-OH exhibited the best intrinsic performance.

Moreover, the robust stability of PO-CoFe-OH was also tested by chronopotentiometry (Fig. 3(f) and Fig. S27 in the ESM). The SEM image, Raman spectra, TEM/HRTEM images, and XRD pattern of PO-CoFe-OH after the stability test also demonstrated the robust structure stability (Fig. S28 in the ESM). We have collected the electrolyte of PO-CoFe-OH after stability test (50 h, 10 mA·cm^{-2} in 80 mL electrolyte) for ICP-OES analysis. The Co and Fe ions concentrations are as low as 0.044 ppm and 0.052 ppm, respectively. The dissolution rate of Co and Fe can be calculated to be as small as 0.070 and 0.083 ug·cm^{-2}·h^{-1}, respectively, revealing the dissolution of Fe and Co can be ignored during the catalytic reaction under mild condition. Because CO_2 reduction is one of the most critical applications for OER, the performance of the catalysts was further evaluated in CO_2-saturated 0.1 M $KHCO_3$ aqueous solution (pH = 6.9), and a current density of 10 mA·cm^{-2} was achieved at an overpotential of 428 mV on PO-CoFe-OH, which is one of the most efficient catalysts among the reported ones (Fig. S29 and Table S4 in the ESM). Amorphous CoFe oxyhydroxide ($Co^{II}_{0.47}Fe^{III}_{0.53}O_xH_y$) on Ni foam was directly prepared for comparison with the PO-CoFe-OH (Figs. S30(a)–S30(d)). The oxidation peak of Co^{2+} is larger in $Co^{II}_{0.47}Fe^{III}_{0.53}O_xH_y$, and it can be attributed to the amorphous structure of $Co^{II}_{0.47}Fe^{III}_{0.53}O_xH_y$ facilitate the oxidation of Co^{2+} [56]. PO-CoFe-OH also gives a better performance than the directly prepared $Co^{II}_{0.47}Fe^{III}_{0.53}O_xH_y$, further verifying the crucial role of partial oxidized state of PO-CoFe-OH.

3.3 Oxygen evolution reaction mechanism

Operando Raman spectra were collected to further understand the outstanding performance of PO-CoFe-OH (Figs. 4(a)–4(d) and Fig. S31 in the ESM). As shown in Figs. 4(b)–4(d), two Raman peaks placed at 400 ~ 500 cm^{-1} originated from the intrinsic structure of CoFe-OH, PO-CoFe-OH, and HO-CoFe-OH are observed at open circuit, which is similar to that observed *ex situ*. Under the bias of 1.3 and 1.5V, the shape of the two peaks shows no change, revealing that the structures are stable under OER in mild condition. In addition, two new Raman peaks at 1,013 and 1,086 cm^{-1}, are clearly observed on PO-CoFe-OH, where no other obvious peak is observed on CoFe-OH and HO-CoFe-OH (Figs. 4(b)–4(d)). The two peaks correspond to the critical surface superoxide intermediate (MOO^-), which reveals that PO-CoFe-OH catalyze through the lattice oxygen oxidation mechanism (LOM) (Fig. 5(a)) [29, 33, 57]. The LOM, involving the direct O–O coupling, can circumvent the limitation provided by conventional adsorbate evolution mechanism (AEM) of highly dependent with the adsorption of the intermediates and give superior performance [29].

An isotope labeling experiment was further performed to understand the OER mechanism. The Raman spectra of PO-CoFe-OH after electrolysis in 0.5 M $H_2{}^{18}O$ and 0.1 M $KHCO_3$ aqueous solution at the current density of 5 mA·cm^{-2} for 10 min shows red shift, implying ^{18}O was incorporated in the lattice of PO-CoFe-OH, and further confirm the LOM of PO-CoFe-OH (Fig. 4(e)). The LOM is strongly correlated with the M-O covalency [29, 51, 58]. Thus, the appropriately strengthened

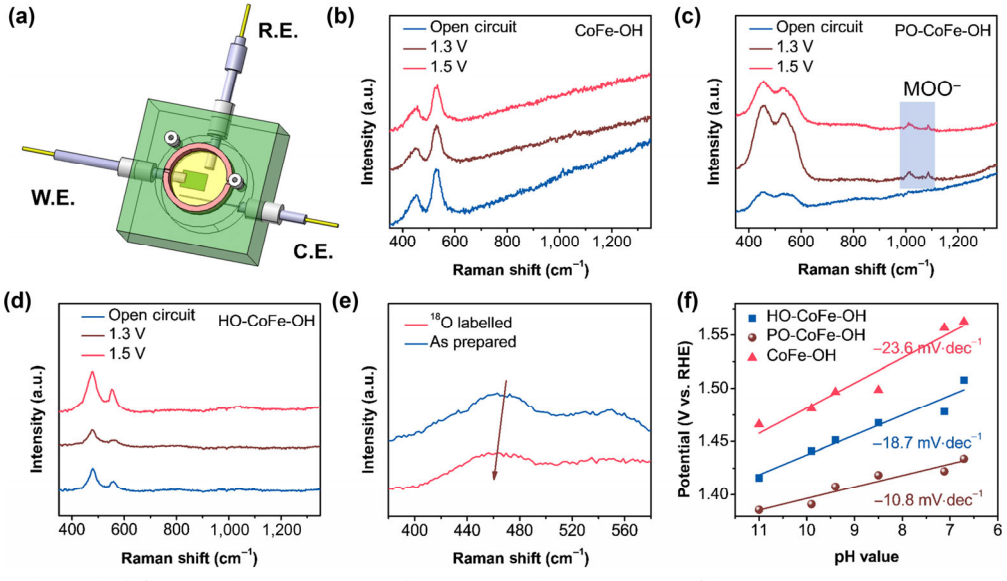

Figure 4 (a) Electrochemical cell for operando Raman spectra collecting. operando Raman spectra of (b) CoFe-OH, (c) PO-CoFe-OH, and (d) HO-CoFe-OH. (e) The Raman spectra of the as prepared PO-CoFe-OH and that after electrolysis in 0.5 M $H_2{}^{18}O$ and 0.1 M $KHCO_3$ aqueous solution at the current density of 5 mA·cm^{-2} for 10 min. (f) The pH-dependent potential of the samples collected at the current density of 0.5 mA·cm^{-2}; the pH of the electrolyte was regulated by mixing 0.05 M K_2CO_3 and CO_2 saturate 0.1 M $KHCO_3$.

M-O covalency in PO-CoFe-OH is highly expectedly responsible for the change of the mechanism and exhibiting superior performance [59]. In addition, due to the rate-determined pH-dependent deprotonation step of LOM, the OER activity is greatly dependent on pH values and usually displayed unsatisfactory performance under (near-)neutral electrolyte [29, 51, 58]. We further evaluate the effects of pH on the activity (Fig. 4(f)). Unexpectedly, we found PO-CoFe-OH gave a more pH-independent activity compared with CoFe-OH and HO-CoFe-OH, revealing the deprotonation step was significantly promoted on PO-CoFe-OH.

DFT + U calculations were employed to calculate the Gibbers free energy of the elementary steps of LOM and AEM to understand the process of OER on PO-CoFe-OH (Figs. 5(a) and 5(c) in the ESM). The models of CoFeOOH/CoFe-OH were established for the representation of PO-CoFe-OH. Similar to the previous reported, Fe^{3+} is considered as the active center for AEM calculation [60–62]. As displayed in Figs. 5(b) and 5(d), the rate-determined step is step 2 for LOM and step 3 for AEM. The values of ΔG_2 for LOM (1.80 eV) is less than that of ΔG_3 for AEM (2.47 eV), revealing that PO-CoFe-OH favors oxygen evolution through LOM.

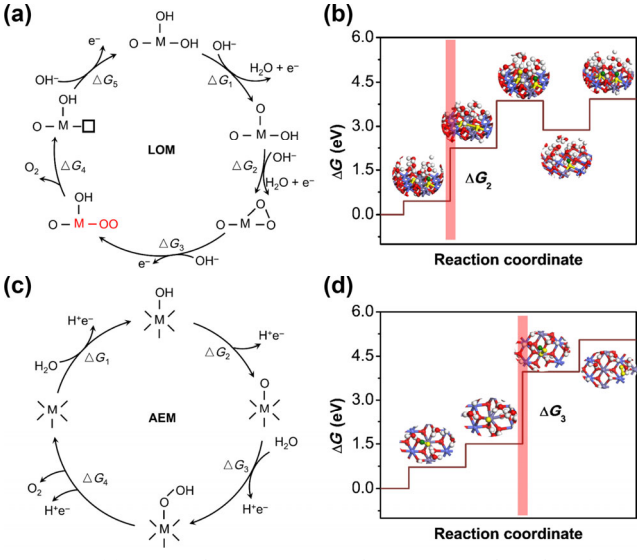

Figure 5 (a) Proposed LOM oxygen evolution process; the red marked is MOO^-. (b) Free energy diagram of PO-CoFe-OH for OER with LOM. (c) Proposed AEM oxygen evolution process. (d) Free energy diagram of PO-CoFe-OH for OER with AEM. O: red, H: white, Co: blue, Fe: dusty blue. Oxygen and hydrogen for reaction are marked as yellow and green, respectively.

4 Conclusions

In conclusion, this paper describes that PO-CoFe-OH gives enhanced performance for OER in mild conditions. The overpotentials at current densities of 1 and 10 $mA{\cdot}cm^{-2}$ are as low as 186 mV and 365 mV, respectively, in 0.1 M $KHCO_3$ aqueous solution (pH = 8.3). Mechanism study reveals that the slightly enhanced M-O covalency in PO-CoFe-OH shifts the OER path from AEM to LOM, and the deprotonation is also promoted, both contribute to the enhanced activity. In addition, we find the oxidation of hydroxide is a general route to strengthen the M-O covalency and boost the OER activity (Figs. S32–S35 in the ESM). It provides a new insight for the preparation of efficient OER catalysts for mild condition electrolysis.

Acknowledgements

We acknowledge the support from the National Natural Science Foundation of China (Nos. 21878202, 21975175, and U1932119), the research project supported by Shanxi Scholarship Council of China (No. 2017-041), the Natural Science Foundation of Shanxi Province (No. 201801D121052), and the National Key Basic Research Program of China (No. 2017YFA0403402).

Electronic Supplementary Material: Supplementary material (the characterizations of CoFe-OH and HO-CoFe-OH: SEM images, TEM images, elemental mapping, EXAFS curves, EIS analysis, CV curves, and additional electrochemical results) is available in the online version of this article at https://doi.org/10.1007/s12274-021-3451-7.

References

[1] Suen, N. T.; Hung, S. F.; Quan, Q.; Zhang, N.; Xu, Y. J.; Chen, H. M. Electrocatalysis for the oxygen evolution reaction: Recent development and future perspectives. *Chem. Soc. Rev.* **2017**, *46*, 337–365.

[2] Hunter, B. M.; Gray, H. B.; Müller, A. M. Earth-abundant heterogeneous water oxidation catalysts. *Chem. Rev.* **2016**, *116*, 14120–14136.

[3] McCrory, C. C. L.; Jung, S.; Peters, J. C.; Jaramillo, T. F. Benchmarking heterogeneous electrocatalysts for the oxygen evolution reaction. *J. Am. Chem. Soc.* **2013**, *135*, 16977–16987.

[4] Ledendecker, M.; Geiger, S.; Hengge, K.; Lim, J.; Cherevko, S.; Mingers, A. M.; Göhl, D.; Fortunato, G. V.; Jalalpoor, D.; Schüth, F. et al. Towards maximized utilization of iridium for the acidic oxygen evolution reaction. *Nano Res.* **2019**, *12*, 2275–2280.

[5] Kanan, M. W.; Nocera, D. G. *In situ* formation of an oxygen-evolving catalyst in neutral water containing phosphate and Co^{2+}. *Science* **2008**, *321*, 1072–1075.

[6] Surendranath, Y.; Kanan, M. W.; Nocera, D. G. Mechanistic studies of the oxygen evolution reaction by a cobalt-phosphate catalyst at neutral pH. *J. Am. Chem. Soc.* **2010**, *132*, 16501–16509.

[7] Dincă, M.; Surendranath, Y.; Nocera, D. G. Nickel-borate oxygen-evolving catalyst that functions under benign conditions. *Proc. Natl. Acad. Sci. USA* **2010**, *107*, 10337–10341.

[8] Yang, L. B.; Liu, D. N.; Hao, S.; Kong, R. M.; Asiri, A. M.; Zhang, C. X.; Sun, X. P. A cobalt-borate nanosheet array: An efficient and durable non-noble-metal electrocatalyst for water oxidation at near neutral pH. *J. Mater. Chem. A* **2017**, *5*, 7305–7308.

[9] Cui, L.; Qu, F. L.; Liu, J. Q.; Du, G.; Asiri, A. M.; Sun, X. P. Interconnected network of core–shell CoP@CoBiPi for efficient water oxidation electrocatalysis under near neutral conditions. *ChemSusChem* **2017**, *10*, 1370–1374.

[10] Ji, X. Q.; Cui, L.; Liu, D. N.; Hao, S.; Liu, J. Q.; Qu, F. L.; Ma, Y. J.; Du, G.; Asiri, A. M.; Sun, X. P. A nickel-borate nanoarray: A highly active 3D oxygen-evolving catalyst electrode operating in near-neutral water. *Chem. Commun.* **2017**, *53*, 3070–3073.

[11] Shao, Y.; Xiao, X.; Zhu, Y. P.; Ma, T. Y. Single-crystal cobalt phosphate nanosheets for biomimetic oxygen evolution in neutral electrolytes. *Angew. Chem., Int. Ed.* **2019**, *58*, 14599–14604.

[12] Zhang, Y. K.; Wu, C. Q.; Jiang, H. L.; Lin, Y. X.; Liu, H. J.; He, Q.; Chen, S. M.; Duan, T.; Song, L. Atomic iridium incorporated in cobalt hydroxide for efficient oxygen evolution catalysis in neutral electrolyte. *Adv. Mater.* **2018**, *30*, 1707522.

[13] Xu, Y. T.; Ye, Z. M.; Ye, J. W.; Cao, L. M.; Huang, R. K.; Wu, J. X.; Zhou, D. D.; Zhang, X. F.; He, C. T.; Zhang, J. P. et al. Non-3d metal modulation of a cobalt imidazolate framework for excellent electrocatalytic oxygen evolution in neutral media. *Angew. Chem., Int. Ed.* **2019**, *58*, 139–143.

[14] Ullman, A. M.; Brodsky, C. N.; Li, N.; Zheng, S. L.; Nocera, D. G. Probing edge site reactivity of oxidic cobalt water oxidation catalysts. *J. Am. Chem. Soc.* **2016**, *138*, 4229–4236.

[15] Zhang, H.; Li, H. Y.; Akram, B.; Wang, X. Fabrication of NiFe layered double hydroxide with well-defined laminar superstructure as highly efficient oxygen evolution electrocatalysts. *Nano Res.* **2019**, *12*, 1327–1331.

[16] Yuan, Z. J.; Bak, S. M.; Li, P. S.; Jia, Y.; Zheng, L. R.; Zhou, Y.; Bai, L.; Hu, E. Y.; Yang, X. Q.; Cai, Z. et al. Activating layered double hydroxide with multivacancies by memory effect for energy-efficient hydrogen production at neutral pH. *ACS Energy Lett.* **2019**, *4*, 1412–1418.

[17] Song, F.; Hu, X. L. Exfoliation of layered double hydroxides for enhanced oxygen evolution catalysis. *Nat. Commun.* **2014**, *5*, 4477.
[18] Li, P. S.; Wang, M. Y.; Duan, X. X.; Zheng, L. R.; Cheng, X. P.; Zhang, Y. F.; Kuang, Y.; Li, Y. P.; Ma, Q.; Feng, Z. X. et al. Boosting oxygen evolution of single-atomic ruthenium through electronic coupling with cobalt-iron layered double hydroxides. *Nat. Commun.* **2019**, *10*, 1711.
[19] Zhao, Y. F.; Zhang, X.; Jia, X. D.; Waterhouse, G. I. N.; Shi, R.; Zhang, X. R.; Zhan, F.; Tao, Y.; Wu, L. Z.; Tung, C. H. et al. Sub-3 nm ultrafine monolayer layered double hydroxide nanosheets for electrochemical water oxidation. *Adv. Energy Mater.* **2018**, *8*, 1703585.
[20] Wang, A. L.; Xu, H.; Li, G. R. NiCoFe layered triple hydroxides with porous structures as high-performance electrocatalysts for overall water splitting. *ACS Energy Lett.* **2016**, *1*, 445–453.
[21] Huang, M. Q.; Liu, W. W.; Wang, L.; Liu, J. W.; Chen, G. Y.; You, W. B.; Zhang, J.; Yuan, L. J.; Zhang, X. F.; Che, R. C. Self-transforming ultrathin α-$Co(OH)_2$ nanosheet arrays from metal-organic framework modified graphene oxide with sandwichlike structure for efficient electrocatalytic oxygen evolution. *Nano Res.* **2020**, *13*, 810–817.
[22] Wang, T. J.; Liu, X. Y.; Li, Y.; Li, F. M.; Deng, Z. W.; Chen, Y. Ultrasonication-assisted and gram-scale synthesis of Co-LDH nanosheet aggregates for oxygen evolution reaction. *Nano Res.* **2020**, *13*, 79–85.
[23] Wang, Y. Y.; Zhang, Y. Q.; Liu, Z. J.; Xie, C.; Feng, S.; Liu, D. D.; Shao, M. F.; Wang, S. Y. Layered double hydroxide nanosheets with multiple vacancies obtained by dry exfoliation as highly efficient oxygen evolution electrocatalysts. *Angew. Chem., Int. Ed.* **2017**, *56*, 5867–5871.
[24] Yu, L.; Zhou, H. Q.; Sun, J. Y.; Qin, F.; Luo, D.; Xie, L. X.; Yu, F.; Bao, J. M.; Li, Y.; Yu, Y. et al. Hierarchical Cu@CoFe layered double hydroxide core-shell nanoarchitectures as bifunctional electrocatalysts for efficient overall water splitting. *Nano Energy* **2017**, *41*, 327–336.
[25] Dionigi, F.; Zeng, Z. H.; Sinev, I.; Merzdorf, T.; Deshpande, S.; Lopez, M. B.; Kunze, S.; Zegkinoglou, I.; Sarodnik, H.; Fan, D. X. et al. *In-situ* structure and catalytic mechanism of NiFe and CoFe layered double hydroxides during oxygen evolution. *Nat. Commun.* **2020**, *11*, 2522.
[26] Feng, C.; Faheem, M. B.; Fu, J.; Xiao, Y. Q.; Li, C. L.; Li, Y. B. Fe-based electrocatalysts for oxygen evolution reaction: Progress and perspectives. *ACS Catal.* **2020**, *10*, 4019–4047.
[27] Du, P. W.; Eisenberg, R. Catalysts made of earth-abundant elements (Co, Ni, Fe) for water splitting: Recent progress and future challenges. *Energy Environ. Sci.* **2012**, *5*, 6012–6021.
[28] Tang, C.; Cheng, N. Y.; Pu, Z. H.; Xing, W.; Sun, X. P. NiSe nanowire film supported on nickel foam: An efficient and stable 3D bifunctional electrode for full water splitting. *Angew. Chem., Int. Ed.* **2015**, *54*, 9351–9355.
[29] Huang, Z. F.; Song, J. J.; Du, Y. H.; Xi, S. B.; Dou, S.; Nsanzimana, J. M. V.; Wang, C.; Xu, Z. J.; Wang, X. Chemical and structural origin of lattice oxygen oxidation in Co–Zn oxyhydroxide oxygen evolution electrocatalysts. *Nat. Energy* **2019**, *4*, 329–338.
[30] Song, F.; Bai, L. C.; Moysiadou, A.; Lee, S.; Hu, C.; Liardet, L.; Hu, X. L. Transition metal oxides as electrocatalysts for the oxygen evolution reaction in alkaline solutions: An application-inspired renaissance. *J. Am. Chem. Soc.* **2018**, *140*, 7748–7759.
[31] Fabbri, E.; Nachtegaal, M.; Binninger, T.; Cheng, X.; Kim, B. J.; Durst, J.; Bozza, F.; Graule, T.; Schäublin, R.; Wiles, L. et al. Dynamic surface self-reconstruction is the key of highly active perovskite nano-electrocatalysts for water splitting. *Nat. Mater.* **2017**, *16*, 925–931.
[32] Stevens, M. B.; Enman, L. J.; Korkus, E. H.; Zaffran, J.; Trang, C. D. M.; Asbury, J.; Kast, M. G.; Toroker, M. C.; Boettcher, S. W. Ternary Ni-Co-Fe oxyhydroxide oxygen evolution catalysts: Intrinsic activity trends, electrical conductivity, and electronic band structure. *Nano Res.* **2019**, *12*, 2288–2295.
[33] Trześniewski, B. J.; Diaz-Morales, O.; Vermaas, D. A.; Longo, A.; Bras, W.; Koper, M. T. M.; Smith, W. A. *In situ* observation of active oxygen species in Fe-containing Ni-based oxygen evolution catalysts: The effect of pH on electrochemical activity. *J. Am. Chem. Soc.* **2015**, *137*, 15112–15121.
[34] Diaz-Morales, O.; Ferrus-Suspedra, D.; Koper, M. T. M. The importance of nickel oxyhydroxide deprotonation on its activity towards electrochemical water oxidation. *Chem. Sci.* **2016**, *7*, 2639–2645.
[35] Görlin, M.; de Araújo, J. F.; Schmies, H.; Bernsmeier, D.; Dresp, S.; Gliech, M.; Jusys, Z.; Chernev, P.; Kraehnert, R.; Dau, H. et al. Tracking catalyst redox states and reaction dynamics in Ni-Fe oxyhydroxide oxygen evolution reaction electrocatalysts: The role of catalyst support and electrolyte pH. *J. Am. Chem. Soc.* **2017**, *139*, 2070–2082.
[36] Bergmann, A.; Jones, T. E.; Martinez Moreno, E.; Teschner, D.; Chernev, P.; Gliech, M.; Reier, T.; Dau, H.; Strasser, P. Unified structural motifs of the catalytically active state of Co(oxyhydr)oxides during the electrochemical oxygen evolution reaction. *Nat. Catal.* **2018**, *1*, 711–719.
[37] Zhong, D. Z.; Zhang, L.; Li, C. C.; Li, D. D.; Wei, C. C.; Zhao, Q.; Li, J. P.; Gong, J. L. Nanostructured NiFe (oxy)hydroxide with easily oxidized Ni towards efficient oxygen evolution reactions. *J. Mater. Chem. A* **2018**, *6*, 16180–16817.
[38] Clark, S. J.; Segall, M. D.; Pickard, C. J.; Hasnip, P. J.; Probert, M. I. J.; Refson, K.; Payne, M. C. First principles methods using CASTEP. *Z. Kristallogr.* **2005**, *220*, 567–570.
[39] Singh, V.; Kosa, M.; Majhi, K.; Major, D. T. Putting DFT to the test: A first-principles study of electronic, magnetic, and optical properties of Co_3O_4. *J. Chem. Theory Comput.* **2015**, *11*, 64–72.
[40] Pack, J. D.; Monkhorst, H. J.; Freeman, D. L. Lithium crystal properties from high-quality Hartree-Fock wave functions. *Solid State Commun.* **1979**, *29*, 723–725.
[41] Monkhorst, H. J.; Pack, J. D. Special points for Brillouin-zone integrations. *Phys. Rev. B* **1976**, *13*, 5188–5192.
[42] Chadi, D. J. Special points for Brillouin-zone integrations. *Phys. Rev. B* **1977**, *16*, 1746–1747.
[43] Chemelewski, W. D.; Lee, H. C.; Lin, J. F.; Bard, A. J.; Mullins, C. B. Amorphous FeOOH oxygen evolution reaction catalyst for photoelectrochemical water splitting. *J. Am. Chem. Soc.* **2014**, *136*, 2843–2850.
[44] Yang, R.; Zhou, Y. M.; Xing, Y. Y.; Li, D.; Jiang, D. L.; Chen, M.; Shi, W. D.; Yuan, S. Q. Synergistic coupling of CoFe-LDH arrays with NiFe-LDH nanosheet for highly efficient overall water splitting in alkaline media. *Appl. Catal. B Environ.* **2019**, *253*, 131–139.
[45] Liu, L.; Jiang, Z. Q.; Fang, L.; Xu, H. T.; Zhang, H. J.; Gu, X.; Wang, Y. Probing the crystal plane effect of Co_3O_4 for enhanced electrocatalytic performance toward efficient overall water splitting. *ACS Appl. Mater. Interfaces* **2017**, *9*, 27736–27744.
[46] Liu, T. Y.; Diao, P. Nickel foam supported Cr-doped $NiCo_2O_4$/FeOOH nanoneedle arrays as a high-performance bifunctional electrocatalyst for overall water splitting. *Nano Res.* **2020**, *13*, 3299–3309.
[47] Ma, L. N.; Zhou, H.; Xu, M.; Hao, P. P.; Kong, X. G.; Duan, H. H. Integrating hydrogen production with anodic selective oxidation of sulfides over a CoFe layered double hydroxide electrode. *Chem. Sci.* **2021**, *12*, 938–945.
[48] Liu, S. J.; Zhu, J.; Sun, M.; Ma, Z. X.; Hu, K.; Nakajima, T.; Liu, X. H.; Schmuki, P.; Wang, L. Promoting the hydrogen evolution reaction through oxygen vacancies and phase transformation engineering on layered double hydroxide nanosheets. *J. Mater. Chem. A* **2020**, *8*, 2490–2497.
[49] Zhu, K. Y.; Chen, J. Y.; Wang, W. J.; Liao, J. W.; Dong, J. C.; Chee, M. O. L.; Wang, N.; Dong, P.; Ajayan, P. M.; Gao, S. P. et al. Etching-doping sedimentation equilibrium strategy: Accelerating kinetics on hollow Rh-doped cofe-layered double hydroxides for water splitting. *Adv. Funct. Mater.* **2020**, *30*, 2003556.
[50] Zhang, J. F.; Liu, J. Y.; Xi, L. F.; Yu, Y. F.; Chen, N.; Sun, S. H.; Wang, W. C.; Lange, K. M.; Zhang, B. Single-atom Au/NiFe layered double hydroxide electrocatalyst: Probing the origin of activity for oxygen evolution reaction. *J. Am. Chem. Soc.* **2018**, *140*, 3867–3879.
[51] Zhao, J. W.; Li, C. F.; Shi, Z. X.; Guan, J. L.; Li, G. R. Boosting lattice oxygen oxidation of perovskite to efficiently catalyze oxygen evolution reaction by FeOOH decoration. *Research* **2020**, *2020*, 6961578.
[52] Frost, R. L.; Weier, M. L.; Kloprogge, J. T. Raman spectroscopy of some natural hydrotalcites with sulphate and carbonate in the interlayer. *J. Raman Spectrosc.* **2003**, *34*, 760–768.

[53] Jiang, S.; Klingan, K.; Pasquini, C.; Dau, H. New aspects of operando Raman spectroscopy applied to electrochemical CO_2 reduction on Cu foams. *J. Chem. Phys*. **2019**, *150*, 041718.
[54] Li, Z. H.; Duan, H. H.; Shao, M. F.; Li, J. B.; O'Hare, D.; Wei, M.; Wang, Z. L. Ordered-vacancy-induced cation intercalation into layered double hydroxides: A general approach for high-performance supercapacitors. *Chem* **2018**, *4*, 2168–2179.
[55] Huang, L. A.; He, Z. S.; Guo, J. F.; Pei, S. E.; Shao, H. B.; Wang, J. M. Photodeposition fabrication of hierarchical layered Co-doped Ni oxyhydroxide ($Ni_xCo_{1-x}OOH$) catalysts with enhanced electrocatalytic performance for oxygen evolution reaction. *Nano Res*. **2020**, *13*, 246–254.
[56] Chen, J.; Xu, G. Z.; Wang, C.; Zhu, K.; Wang, H. X.; Yan, S. C.; Yu, Z. T.; Zou, Z. G. High-performance and stable silicon photoanode modified by crystalline Ni@amorphous Co core–shell nanoparticles. *ChemCatChem* **2018**, *10*, 5025–5031.
[57] Zhang, M.; de Respinis, M.; Frei, H. Time-resolved observations of water oxidation intermediates on a cobalt oxide nanoparticle catalyst. *Nat. Chem*. **2014**, *6*, 362–367.
[58] Grimaud, A.; Diaz-Morales, O.; Han, B. H.; Hong, W. T.; Lee, Y. L.; Giordano, L.; Stoerzinger, K. A.; Koper, M. T. M.; Shao-Horn, Y. Activating lattice oxygen redox reactions in metal oxides to catalyse oxygen evolution. *Nat. Chem*. **2017**, *9*, 457–465.
[59] Ye, Y. F.; Thorne, J. E.; Wu, C. H.; Liu, Y. S.; Du, C.; Jang, J. W.; Liu, E.; Wang, D. W.; Guo, J. H. Strong O 2p-Fe 3d hybridization observed in solution-grown hematite films by soft X-ray spectroscopies. *J. Phys. Chem. B* **2018**, *122*, 927–932.
[60] Stevens, M. B.; Trang, C. D. M.; Enman, L. J.; Deng, J.; Boettcher, S. W. Reactive Fe-sites in Ni/Fe (oxy)hydroxide are responsible for exceptional oxygen electrocatalysis activity. *J. Am. Chem. Soc*. **2017**, *139*, 11361–11364.
[61] Ahn, H. S.; Bard, A. J. Surface interrogation scanning electrochemical microscopy of $Ni_{1-x}Fe_xOOH$ ($0 < x < 0.27$) oxygen evolving catalyst: Kinetics of the "fast" iron sites. *J. Am. Chem. Soc*. **2016**, *138*, 313–318.
[62] Friebel, D.; Louie, M. W.; Bajdich, M.; Sanwald, K. E.; Cai, Y.; Wise, A. M.; Cheng, M. J.; Sokaras, D.; Weng, T. C.; Alonso-Mori, R. et al. Identification of highly active Fe sites in (Ni, Fe)OOH for electrocatalytic water splitting. *J. Am. Chem. Soc*. **2015**, *137*, 1305–1313.